Received: 12 July 2025 | Revised: 8 August 2025 | Accepted: 12 August 2025

DOI: 10.1111/jmi.70027

Journal of Microscopy RMS

ORIGINAL ARTICLE

Quantitative corrections for fluctuation electron microscopy

J. M. Gibson[1] | **M. M. J. Treacy**[2]

[1]Department of Mechanical Engineering, FAMU-FSU College of Engineering, Tallahassee, Florida, USA

[2]Department of Physics, Arizona State University, Tempe, Arizona, USA

Correspondence
J.M. Gibson, Department of Mechanical Engineering, FAMU-FSU College of Engineering, 2525 Pottsdamer St., Tallahassee, FL 32310.
Email: jmgibson@eng.famu.fsu.edu

Funding information
National Science Foundation, Grant/Award Numbers: 1906367, DMR-2128556

Abstract

Anomalously low values of the normalised variance in fluctuation electron microscopy (FEM) have been frequently reported. We present three experimental corrections for quantitative interpretation that significantly modify conventional approaches. FEM relies on measurements of intensity statistics in coherent nanodiffraction patterns. We demonstrate that sampling the nanodiffraction patterns with a pixelated detector removes high-frequency signals and reduces statistical variance. The most significant impact is on the background normalised variance, which arises from random atomic alignments and is distinct from the normalised variance peaks associated with the correlated alignments of medium-range order. Indeed, we show that if the peaks are background-subtracted, their height is much less affected by the detector effect, provided the experimental conditions are optimised. We show that shot noise correction must also be adjusted to account for the camera Modulation Transfer Function (MTF) effects. Additionally, we demonstrate through experiment that the traditional method of thickness correction for a-Si is inadequate and propose an alternative approach to address thickness variations. We speculate on the origin of the anomalous thickness effect in terms of displacement decoherence due to sample 'fluttering' under irradiation.

KEYWORDS

4D-STEM, amorphous materials, medium-range order, scanning transmission electron microscopy (STEM), transmission electron microscopy (TEM)

1 | INTRODUCTION

Fluctuation electron microscopy (FEM) is widely used to examine medium-range order (MRO) in amorphous materials.[1–7] It has been well recognised that the absolute value of the measured FEM normalised variance is lower than that predicted by theory and simulation.[8] Several factors have been considered to explain this, including partial coherence in the illumination,[9] specimen drift, atom motions attributed to the electron beam (displacement decoherence),[8] charging,[8] and inelastic scattering.[10] It is likely that many of these factors contribute to the reduced variance but, in this paper, we explore some effects on FEM normalised variance measurements that have not been adequately explored – the finite pixelation of a detector, and the detector (camera) Modulation Transfer Function (MTF). Our work builds on recent work by Zjajo et al., who examined the effects of electron counting in adjacent pixels within a hybrid pixel direct electron detector.[11] We also report a complex and intriguing dependence of the FEM signal on thickness in amorphous Si and discuss the origin. For each of these challenges, we elucidate approaches to compensate for, or at least minimise, artefacts when comparing experimental measurements with simulations or data from other samples.

The effect of the camera point spread function (the Fourier transform of the MTF) on the resolution of an image has been well-studied and is readily corrected.[12] However, we show here a large effect from the MTF that has hitherto been overlooked but has recently drawn attention to hybrid-pixel array cameras.[11] The statistical impact of 'pixel sharing' is found to be substantial for the typical optically coupled CCD or CMOS cameras used in FEM, especially concerning the reduced background observed in the normalised variance. We describe the effect using simulations and explain how to compensate for it. In addition, we show how the camera MTF effect can complicate the important subtraction of electron shot noise and describe an approach to correct for this. Finally, we are reassured that if experimental data are acquired appropriately, the pixelation effect need not significantly affect the interpretation of medium-range order peaks; however, these should be reported relative to the background and not with respect to the $V = 0$ axis.

The introduction in the last few years of direct electron detectors, such as active pixel sensors[13] and hybrid pixel arrays,[14] offers great advancements in FEM quantitation. Nevertheless, the majority of published FEM data used optically coupled CCD or CMOS detectors and it is important to understand the effects of these detectors in evaluating those results. Also, it will likely take some time until all microscopy facilities have access to the new detectors. Furthermore, while the new detectors are much improved and may in some case have no point spread to adjacent pixels, they still suffer from the fundamental effects of pixelation on FEM statistics that we introduce here, and our recommendations for data analysis are equally relevant.

FEM measures the normalised statistical variance of an ensemble of coherent nanodiffraction patterns as a function of reciprocal lattice vector amplitude q and probe size R:[15]

$$V(q,R) = \left\langle \frac{\left\langle I_{\vec{r}}^2(\vec{q},R)\right\rangle}{\left\langle I_{\vec{r}}(\vec{q},R)\right\rangle^2} \right\rangle_{\Phi} - 1. \qquad (1)$$

The nanodiffraction patterns, $I_{\vec{r}}(\vec{q},R)$, collected using a probe of resolution R at various positions $\vec{r}$ across the sample are averaged to give the mean diffraction pattern, $\langle I_{\vec{r}}(\vec{q},R)\rangle$. The square of the diffraction pattern intensities, the second moment of intensity, is also averaged to provide, $\langle I_{\vec{r}}^2(\vec{q},R)\rangle$. Without further averaging, these two terms would yield a 2-dimensional normalised variance pattern, $V(\vec{q},R)$, (ignoring the subscript ϕ in (1)). Since most amorphous materials are isotropic, it is convenient to further average the normalised variance over the azimuthal angle, ϕ with respect to the diffraction origin, to produce a 1-dimensional normalised variance plot. As pointed out by Daulton et al.,[3] there are several mathematically distinct ways to accomplish azimuthal averaging. Daulton identified four, and Zjajo et al. described a fifth variant.[11] Here, we use Daulton's fourth method, the 'annular mean of variance image'.

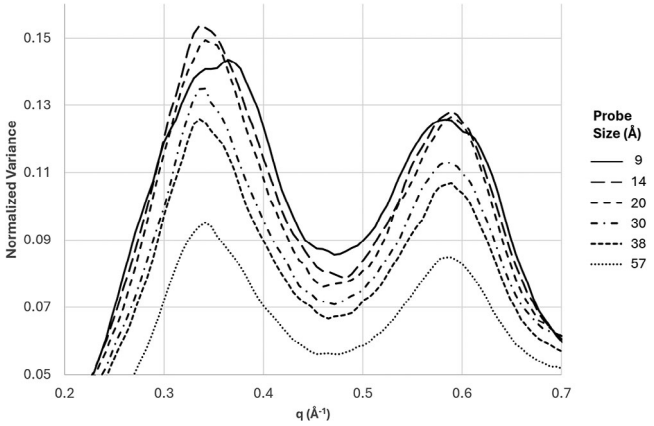

FIGURE 1 Typical raw normalised variance experimental data for a 50 Å thick sputtered amorphous Si film. The electron fluence at 60 keV is held relatively constant. Note the probe size dependence in the background level at the dip near 0.47 $Å^{-1}$.

FEM theory predicts that the normalised variance $V(q,R)$ from a fully random sample should have a value of unity at all values of reciprocal lattice vector magnitude q and probe size (resolution) R. It is also clear from simulations that MRO produces peaks in $V(q,R)$ but between the peaks (at the dips) V returns to a value close to unity.[4,16] We refer to this value as the background level. In practice, the experimental background values are often less than 0.1.

Figure 1 shows experimental FEM normalised variance data taken with 60 keV electrons from a 50 Å thick sputtered amorphous Si membrane commercially available from SPI®. The data shown is raw and has not been corrected for shot noise, although at these exposures and q values, the shot noise contribution is small. Note how the 'background' dip at about 0.47 $Å^{-1}$ (between the 0.31 $Å^{-1}$ and 0.57 $Å^{-1}$ MRO peaks) has a normalised variance level much less than 1.0 and decreases monotonically as the probe size increases.

Partial illumination coherence, displacement decoherence, and inelastic scattering are factors contributing to background attenuation. However, these are likely not sufficient to explain the entire effect, which is still observed in very thin samples where inelastic scattering is small, and with almost fully coherent illumination.[8,10]

2 | MATERIALS AND METHODS

This work focuses on the proper procedure for making reliable measurements of MRO with FEM, specifically three previously unexamined aspects that require important corrections during the experiment and analysis to ensure robust conclusions. Two of these conclusions involve the role of the detector pixelation and MTF on statistical measurements of normalised variance, and correction for electron shot noise. The simulations were carried out using Mathematica®, and the code can be made available by contacting the corresponding author. Relevant details of the simulations are described below.

Experimental data are used to compare with the simulations, taken either at 60 keV electron energy on the aberration-corrected Nion SuperSTEM at the University of Vienna, Faculty of Physics, or (mostly) at 80 keV with the JEOL ARM200F probe-corrected STEM at the National High Magnetic Field Laboratory in Tallahassee, Florida. Both instruments have cold field-emission guns. Simulations show little difference in the FEM normalised variance measurements at these two voltages. The simulations in the figures were carried out for 80 keV electrons, replicating a 256 × 256 detector.

The camera used to record the 80 keV data is the Gatan Orius SC200D optically coupled CCD with 2048 × 2048 pixels, with pixel linear dimension 7.4 μm. The 60 keV data was recorded with a Hamamatsu ORCA Flash 4.0 V3 optically coupled CMOS camera with 2048 × 2048 pixels, with pixel linear dimension 6.5 μm. In both cases, images were binned ×4 to 512 × 512 to reduce shot noise and increase dynamic range. For both detectors, the pixel size in reciprocal space was close to 0.005 $Å^{-1}$.

3 | RESULTS AND DISCUSSION

This section is divided into three subsections based on the three primary conclusions, and the results and discussion are similarly divided for efficiency: correction for pixelation and camera MTF; shot noise correction; and thickness correction.

4 | CORRECTION FOR PIXELATION AND CAMERA MTF

To explore the anomalously low background issue, we have carried out simulations that include the effect of the camera pixelation and MTF. In this initial set of calculations, we disregard shot noise, which we address in the subsequent section. The normalised variance was calculated for two atomic models: (a) a pseudorandom array of atoms at the same density as a-Si; (b) 67% by volume 11.5 Å diamond-structure Si crystallites embedded in a Continuous Random Network (CRN) and relaxed.[17] The latter model is an example of the paracrystalline structure. Each model is a 70 Å cube containing approximately 16,500 atoms, randomly rotated and cut to a thickness of 50 Å. Fast Fourier transforms with a sampling array size 256 × 256 were used in the FEM simulations. Calculations were made for 80 keV electrons, at various probe sizes (Gaussian-shaped probes whose size is defined by the Rayleigh criterion[17]). We assume fully coherent illumination and a stable and stationary set of sampled atoms.

As expected, Figure 2a shows that the unbinned variance (binning factor 1) fluctuates around the average value of unity beyond the cutoff associated with the unscattered-beam near the origin.

Binning well approximates the effect of a larger pixel size. We simulate the effect of binning by a factor of n in Figure 2a for a probe size of 20 Å with the random model, where we see that the normalised variance drops as the effective pixel size doubles with each increase of the binning factor. We can understand this as the removal of spatial frequencies from the electron wavefront as the diffracted intensity is detected, or equivalently, as effective incoherence introduced by a finite-size source through the reciprocity principle. We note that binning smaller pixels is not necessarily equivalent to the result with larger pixels. With binning, we are adding the modulus squared of the wavefunctions detected at each neighbouring pixel (incoherent addition), whereas in larger pixels, those parts of the scattered wavefunction are being 'added' coherently first, then the modulus squared is detected (coherent addition). However, we believe the difference is negligible.

Figure 2b summarises the dependence of the binning effect on probe size for the random model. The larger probe sizes R, which produce finer-scale Fourier space speckles of characteristic width $\sim 1/R$, decay faster, consistent with experiment (Figure 1).

Because we are using a discrete Fourier transform, we are not cutting off any information when the pixel size in reciprocal space is $1/2L$ (L is the model width) – the information limit. In this artificially periodic system with no binning, we collect all the scattered radiation, and the background level is unity as predicted. However, any real detector, even one that collects all electrons and has no 'leakage' between adjacent pixels (i.e. the point spread function is a delta function), has a finite pixel size, which would reduce the background level similarly to the binning effect seen in Figure 2a. The degree of reduction depends on the spatial frequency distribution of the scattering. By increasing the camera length in the microscope, we demagnify the reciprocal space pixel size and reduce

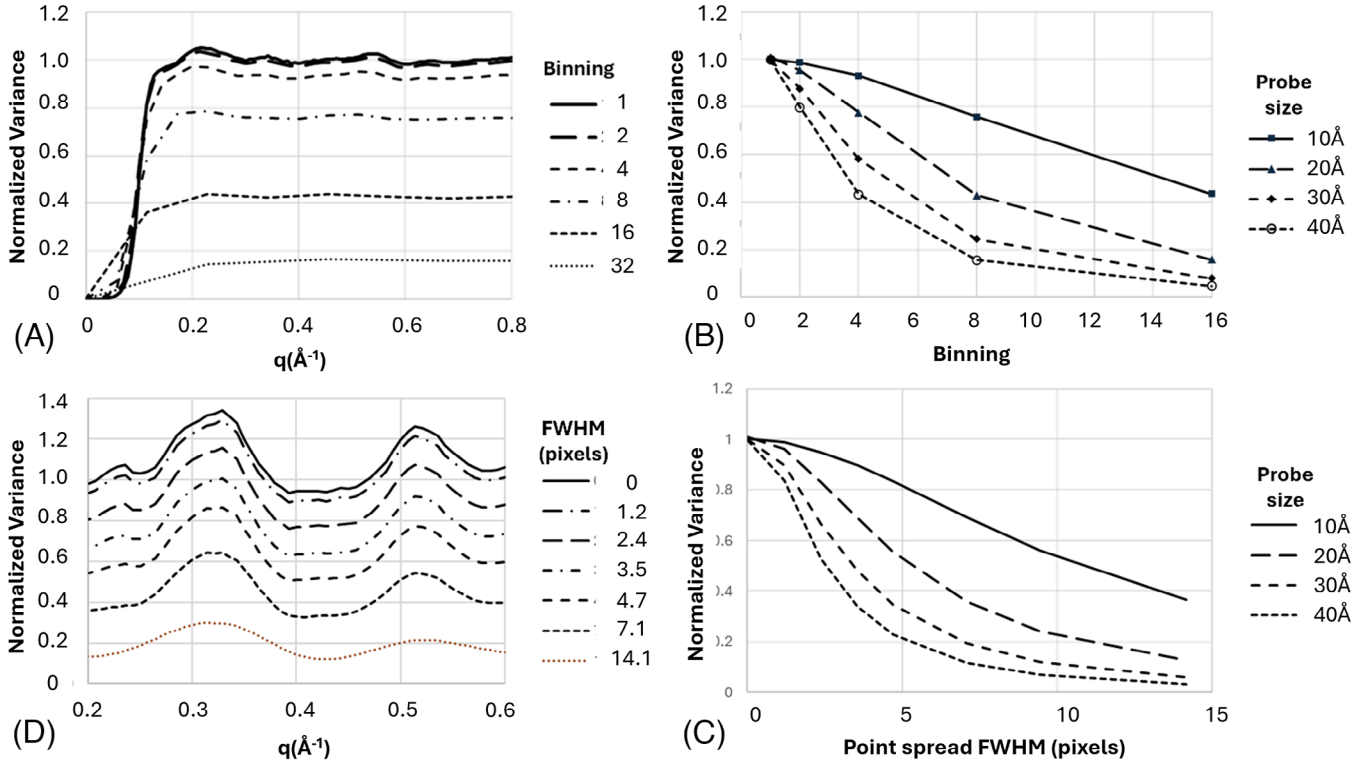

FIGURE 2 Simulations of the FEM normalised variance without shot noise. The reciprocal space pixel is 0.00357 $Å^{-1}$: (a) The dependence on the camera binning factor for a random sample at a probe size of 20 Å. (b) Probe size dependence of the binning effect for the random sample. (c) Normalised variance vs the FWHM (=2.35σ) of the camera point spread function, in pixels, using a 20 Å probe. The trend reflects the experimental results in Figure 1. (d) The diamond paracrystalline composite normalised variance as a function of point spread function FWHM for various probe sizes.

the filtering effect, but this comes at the expense of increasing the Poisson shot noise in each pixel, so there is an optimum camera length. The critical sampling frequency in the detector is determined by the characteristic structural correlation length. Provided structural information is preserved by the detector, we can estimate reliably the peak heights associated with MRO by subtracting the background.

The effect of the point spread function FWHM is like that of binning. For optically coupled cameras, common in most published applications of FEM, the point spread function is usually far broader than one or two pixels because of light leakage. In our simulations, we use a Gaussian model for the camera point spread function, but we truncate the distribution at twice the standard deviation (σ). The functional form is not essential for our conclusions, and truncation reduces simulation time and minimises edge effects. (In reality, the PSF is not a Gaussian, and often has very long tails in optically coupled cameras.[12])

Figure 2c shows the normalised variance from the random sample as a function of the Gaussian FWHM ($\approx 2.35\sigma$) in reciprocal lattice pixel units (for direct comparison with the binning factor). Each pixel in the nanodiffraction patterns corresponds to a reciprocal space width of 0.00357 $Å^{-1}$ (equivalent to a real space periodicity of 140 Å). We observe that the half-height for the background variance ($V_{1/2}$) occurs at the point spread standard deviation $\sigma \approx 1.1/R$, where R is the probe size in Å and σ is in $Å^{-1}$. Note that in Figure 2a–c, each for the random model, there are no peaks in the normalised variance versus reciprocal lattice vector magnitude q, and so we display the average (background) value as a function of binning or FWHM.

Figure 2d shows a series of calculations for a model with medium-range order – the paracrystalline model b described above. The normalised variance is plotted versus reciprocal lattice vector magnitude q for different values of the camera point-spread FHWM. The peaks at 0.31 Å and 0.57 Å are characteristic of the diamond-like medium-range order present in this model. The images were calculated for a probe size of $R = 20$ Å.

The peaks and background are affected differently by the detector point-spread function. In Figure 3, we pull out the 0.31 $Å^{-1}$ background-subtracted peak height (**P-B**), from the paracrystalline model as a function of the point-spread function FWHM. We can see how **P-B** is less affected by the

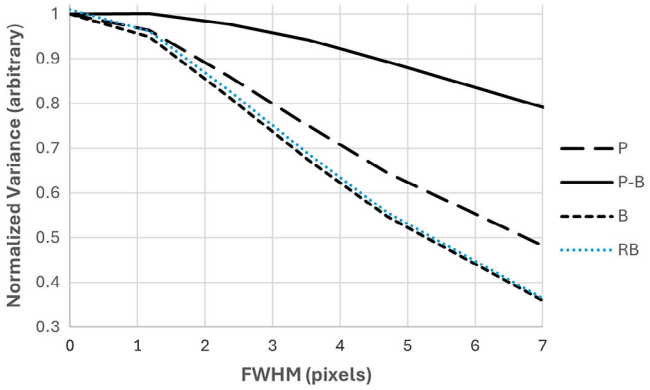

FIGURE 3 The simulated 0.31 Å^{-1} peak height and background for the paracrystalline diamond model with a 20 Å probe as a function of the FWHM of the point spread function (2.35σ). **P** is the raw peak height, **B** the background, and **P-B** the more robust background-subtracted peak height. **RB** is the background under the same conditions from a random sample, which is almost identical. (Note all curves are normalised to 1 at FWHM 0 to ease comparisons.)

camera MTF than the raw peak height **P**. For example, at FWHM 3 pixels **P-B** is reduced by less than 5% while **P** itself is attenuated by ~20%. Significant reduction of **P-B** occurs once the FWHM approaches the scale of the correlation length of the paracrystals, which is 11.5 Å. For example, at FWHM = 7 pixels, or 0.025 Å^{-1}, the Fourier filtering removes periodicities of 40 Å or longer in real space, and **P-B** is attenuated by only 20% (**P** is attenuated by 65%). This suggests that for 20% accuracy, or better, in **P-B** we should work with FWHM about ¼ of the reciprocal correlation length, or smaller.

As a practical example, the FWHM measured experimentally at 80 keV for our Gatan Orius® 2048 × 2048 camera is approximately 8 pixels which at the camera length used to record FEM corresponds to 0.0062 Å^{-1}. This is equivalent to a real-space distance of 80 Å, about 4–6 times the structural correlation length in a-Si (inferred from previous FEM studies[10,18]) and so not likely to greatly affect the measurement of **P-B**.

These results lead to the conclusion that reporting the background-subtracted peak height is a more robust measurement of the normalised variance values associated with medium-range order. This concurs with Zjajo et al.[11] who noted in their study of rapid-acquisition FEM that the normalised variance background was disproportionately suppressed by decoherence relative to the peaks from medium-range order.[11] Since the background changes with q and can only be estimated directly at the 'dips' in a few places, in experimental data we interpolate a smooth curve through these low-variance points and use that as an estimate of the background to be subtracted.

5 | SHOT NOISE CORRECTION

In FEM experiments, one must consider noise, which is often dominated by the quantum nature of electrons. The counting of electrons leads to shot noise, which follows a Poisson distribution in the incident illumination. This noise can be readily incorporated into the FEM simulations.[11] Other sources of noise also occur, such as readout noise, but we have found these to be less critical in FEM data analysis. Since shot noise is pervasive and usually significant with the low-signal data of FEM, it is important to understand the impact of pixelation and MTF on the subtraction algorithm that is commonly used in FEM:[2,19]

$$V(q,R) = \left\langle \frac{\left\langle I_{\vec{r}}^{2}\left(\vec{q},R\right)\right\rangle}{\left\langle I_{\vec{r}}\left(\vec{q},R\right)\right\rangle^{2}} \right\rangle_{\Phi} - 1 - \frac{a}{\left\langle I_{\vec{r}}\left(\vec{q},R\right)\right\rangle_{\Phi}}, \quad (2)$$

where, with a perfect detector, $a = 1$. This approach is based on the Poisson counting characteristic, which states that the variance of the number of events, n, equals the mean, that is, $\langle n^2\rangle - \langle n\rangle^2 = \langle n\rangle$. For the soft x-ray version of FEM, using a zone plate to form the probe, the simple correction identified by Fan et al.[2,19] (with $a = 1$) worked well to remove low levels of noise and reproduce the noise-free model signal. Not so for optically coupled electron detectors that have been most often used in FEM. Equation (2) works well in FEM simulations but not on FEM data. In practice, when $a = 1$ is set, negative values of V arise, especially for high q.[11] Experimentally, we find that values of $a < 1$ work well to bring the high-q FEM normalised variance to a constant level, as it should be after removing shot noise. The recent work by Zjajo et al.[11] points to the reason for this discrepancy: pixel sharing due to the camera point spread function. We extend this idea to the case of more conventional cameras with significant point spread functions far beyond 1 or 2 pixels.

The simulations in Figure 4 are from the same paracrystalline model used in Figure 2d. The mean electron fluence is 6 electrons per pixel at 0.31 Å^{-1}. The elastically scattered intensity for this 50 Å thick sample at this spatial frequency is 1.55×10^{-4}, so that the fluence of electrons in this simulated 20 Å probe is approximately 39,000. In Figure 4a, we show the model signal (with an infinite number of electrons) compared with the 'raw' signal. The noise in the normalised variance increases with q because of the rapid decay of the scattering amplitude with q.

Problems occur with the shot-noise correction algorithm as the point-spread function of the camera is introduced. Figure 4b shows the case where the FWHM of the point-spread function is 1.2 pixels in the nanodiffraction pattern. In this case, while it is not shown, using

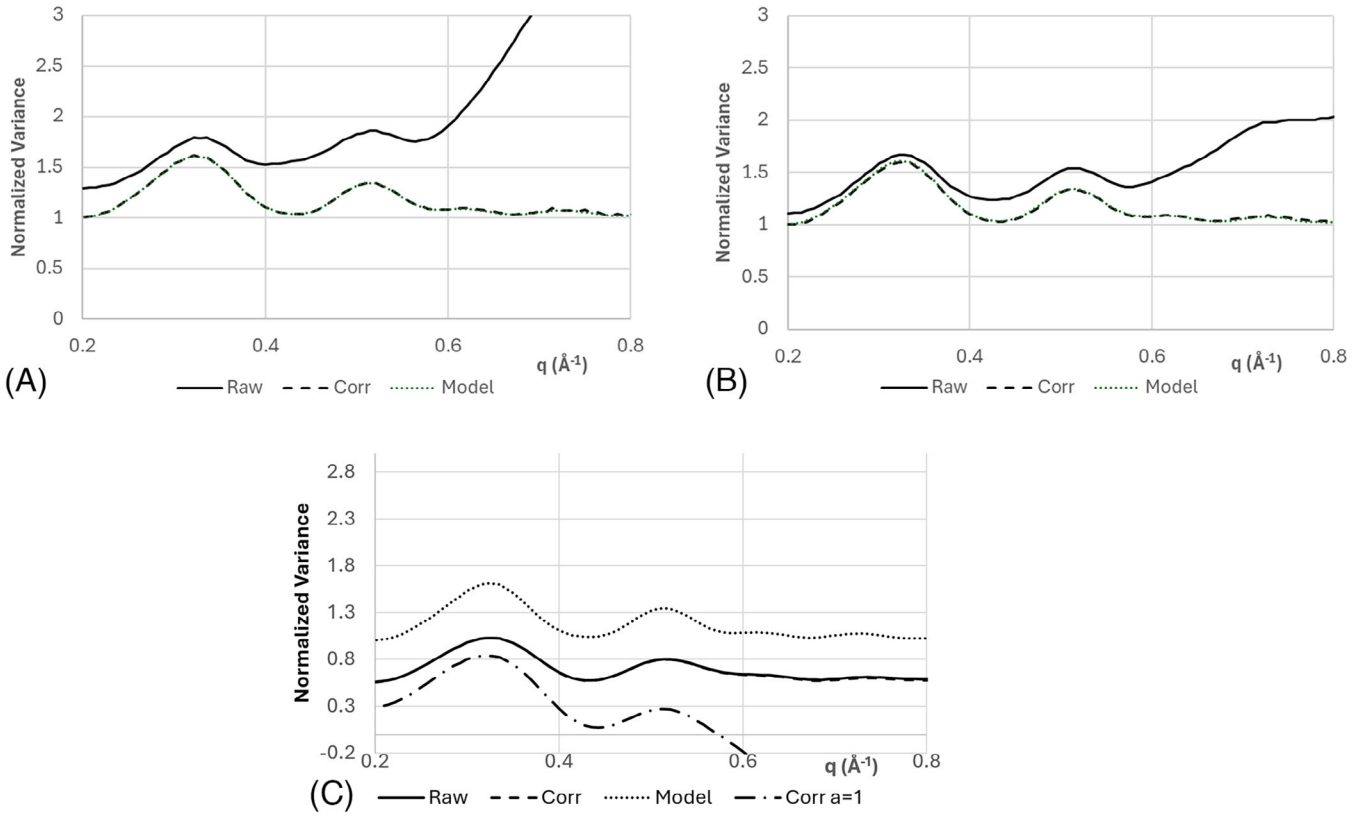

FIGURE 4 The simulated effect of camera point spread function FWHM on shot noise correction. Each graph shows the normalised variance with shot noise from the paracrystallite model with 67% 11.5 Å crystals. **(a)** FWHM = 0: correction factor $a = 1$ brings noise-corrected data (Corr) and model (with no noise) into agreement (curves are superposed). **(b)** FWHM = 1.2 pixels = 0.0042 Å^{-1}. The correction factor $a = 0.4$ removes noise and replicates the model but is shifted slightly to lower V as expected from the last section. **(c)** FWHM= 7.1 pixels = 0.025 Å^{-1}. The corrected variance is obtained with $a = 0.0094$ and is similar to the model but displaced downwards significantly. We also show the effect of using $a = 1$ here, which creates negative variance at many values of q and clearly overcorrects the shot noise. It is also clear that the averaging effect of the camera MTF greatly reduces the shot noise.

$a = 1$ (the value expected for Poisson noise) overcorrects for the noise. By trial and error, we find that a correction factor $a = 0.4(\pm 0.01)$ effectively removes the noise over the range of q plotted. The corrected signal and the model are then well matched except for a slight reduction in background explained in the previous section. With an FWHM of 7.1 pixels (=0.025 Å^{-1}, equivalent to a real space periodicity of 40 Å and more typical of experiment) in Figure 5c, we observe that good correction occurs when $a = 0.0094$. The corrected signal removes the runaway noise at high q(beyond the range of the graph), but still displays the attenuation of the peak height and background predicted even for an infinite number of electrons. For the purpose of illustration, we also show in Figure 4c, the effect of setting $a = 1$, which overcorrects the noise contribution leading to negative values for variance, as has previously been noted.[11]

To understand the origin of the empirical constant a, we consider the integrated value, p, under our point spread function. Setting a value of 1 at the origin of the point spread function, for the case of FWHM = 1.2 pixels, this integral is $p = 1.64$. In this case, the correction factor is $a = 0.6/p$. For the case of FWHM 7.1 pixels, the integral is $p = 94.0$, and the correction factor is $a = 0.5/p$. In general, we find for large FWHM, $a = 0.5/p$, but at small FWHM this increases slightly. We can explain the p dependence of the correction factor as representing the contribution of nearby pixels to the centre pixel, which effectively increases the number of discrete counts and so reduces the shot noise. The correction factor $a = 0.5/p$ represents the multiplicative factor that converts measured counts per pixel into the effective number of real counts. This correction factor works well for broad point-spread functions because each pixel exhibits a similar spread even for low incident counts. However, for narrow point-spread functions, the statistical variation in spread pattern between individual pixels requires a more sophisticated treatment.[11]

The integral under the point spread function p could be obtained separately from measurements on the CCD camera[12] and represents a multiplier on the actual number

of electrons contributing to the signal in each pixel, which controls the noise level. For example, if there are only 6 electrons counted in one pixel in a CCD, with point spread function as in Figure 1c, there are really $6p = 564$ electrons contributing to that pixel (coming from many adjacent pixels). So, instead of a noise % which would appear to be $1/\sqrt{6} = 41\%$, it is actually $1/\sqrt{564} = 0.042\%$, which is almost negligible.

In practice, it is relatively easy to determine the shot-noise correction factor empirically by adjusting a to make the $V(q)$ flat at relatively high q where it tends to run away due to increasing shot noise on the weaker signal. Because of the large practical values of FWHM for CCD and CMOS cameras, the effect of shot noise removal is very small at low q.

We note that the peak heights are strongly affected by noise subtraction; however, the background-subtracted peak height remains more robust until the point spread function impinges on the atomic correlation length scale, as discussed previously. The implication is that the background level is notoriously dependent on many variables, especially the camera's MTF; however, the peak heights when reported relative to the background are more robust. This is consistent with the previous practice of keeping the experimental parameters, such as fluence, constant in the nanodiffraction patterns to reduce the variability of the background. Nevertheless, the better approach is to subtract the background and remove the noise appropriately. We note that some event-driven direct electron detectors can effectively eliminate the point-spread function[20] and so should allow correction of shot noise with $a = 1$ in equation (2).

6 | THICKNESS CORRECTION

Simulations have shown that when the thickness is reasonably small compared to the mean-free-path for elastic scattering, the normalised variance always decreases with increasing thickness, and at non-negligible concentrations it is proportional to $1/t$.[16] This inverse-t dependence makes sense because at greater thicknesses, there are more MRO domains in a column equal to the probe size in width. Assuming uncorrelated domains, the variance $(\langle I^2\rangle - \langle I\rangle^2)$ grows linearly with the number of random domains, which scales with t, whereas the normalising factor, $\langle I\rangle^2$, in the denominator scales as t^2. This has been experimentally verified in some cases[5] but not in others.[3] Of course, the simulations assume fully coherent illumination, with a static set of atoms, and omit decoherence.[8] We have made measurements of a large number of amorphous silicon samples prepared under different conditions[18] – including sputtering, ion implantation, and annealing – and measured the background-subtracted peak variance at a probe size of 27 Å at the first a-Si characteristic peak at 0.31 $Å^{-1}$. The results from 11 different samples are presented as a scatter plot in Figure 5. The variance was measured at typically between three and five different thicknesses for each sample in the plot. The thickness was determined by the average scattered intensity into a ring from 0.2–0.4 $Å^{-1}$. The points from each of the j datasets from sample i were plotted as $(t_{ij}, \alpha_i\ V_{ij})$ in Figure 5, where α_i was chosen to bring all the sets into approximate alignment, revealing the global thickness trend. An example of data contributions from one sample are highlighted with red circles. While the predicted inverse-t dependence is seen above ~200 Å thickness, in thinner samples we observe a variance that grows with thickness.

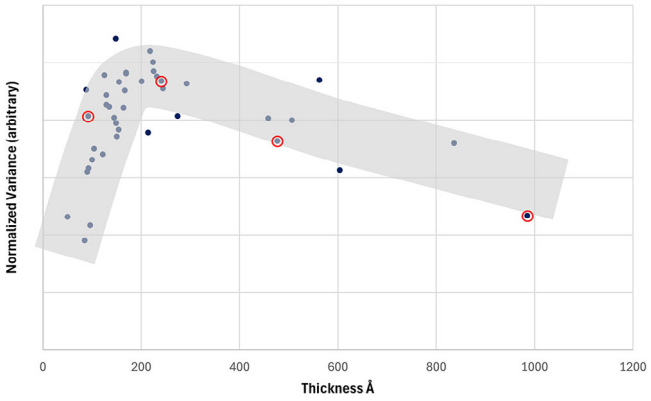

FIGURE 5 A normalised scatter plot of the thickness dependence of the 0.31 $Å^{-1}$ peak over background at a probe size of 27 Å for 11 different amorphous Si samples. The four points with (red) circles are an example of one of the samples. All the data was overlapped using an arbitrary normalised variance multiplier to reveal the general trend with thickness.

While these results may point to the merits of using samples > 200 Å thick (for a-Si), the disadvantage to this is poorer signal-to-noise, and more unwanted contributions from inelastic and plural scattering. We will discuss later the origin of this unexpected thickness effect. From a practical point of view, the best approach for materials of the same composition is to restrict the thicknesses to a narrow range when comparing samples processed in different ways. In recent work on self-ion implanted amorphous silicon,[18] we used measurements at several thicknesses to extrapolate for each sample to a fixed thickness (200 Å) and compared samples with different preparations at the same thickness to ensure reliable comparisons.

It is not clear if the results here are intrinsic to amorphous Si, since others have not reported such a turnaround at low thickness, for example, for metallic glasses.[3,5] Zjajo et al. noted that their background-subtracted a-Si variance peak data did not scale as $1/t$ for thin samples at 50 Å, 90 Å,

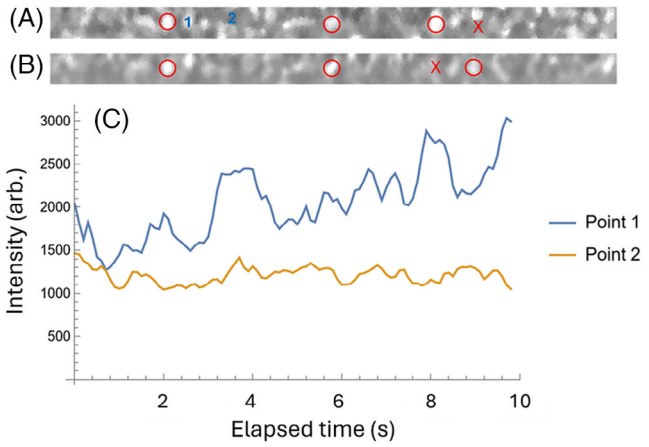

FIGURE 6 **(a, b)** Two azimuthal polar plots showing speckles on the 0.31 Å^{-1} ring (0.26–0.34 Å^{-1}) from individual electron nanodiffraction patterns taken 1.25 s apart from the same area of a 5 nm thick sputtered a-Si sample at 60 keV. Some individual speckles are seen in both patterns (o o), others in only one (x o). **c)** a time scan of a bright speckle (1) and a dark speckle (2) showing the twinkling where the bright speckle can disappear and reappear. Pictures were taken with 50 ms exposure every ~ 90 ms.

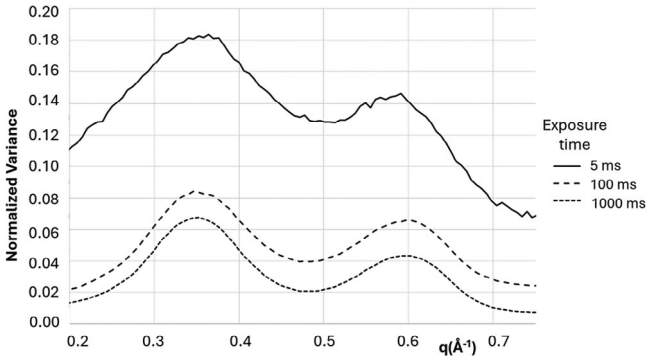

FIGURE 7 FEM variance plots taken from the same region of a sputtered 50 Å thick a-Si film with increasing exposure time from 1 ms to 1000 ms (18 Å probe size), recorded with 60 keV electrons.

and 150 Å thicknesses.[4] Other published measurements have not focused on films of such low thickness, instead choosing thicknesses in the range above 240 Å[5] or more.[3]

Amorphous Si films that have been exposed to air develop a thin amorphous oxide layer. That layer will have its greatest impact on the thinnest samples. However, as Figure 5 shows, reducing t by a fixed offset to correct for the oxide layer does not correct the issue. Note that all our Si samples were prepared by chemical thinning in HF, which leaves a native oxide about 10 Å thick on both surfaces.[21] The total amount of oxide at ~20 Å is ten times smaller than the turning point in the FEM variance versus thickness that we observe.

It is interesting to speculate on the origin of the reversal in predicted $1/t$ behaviour at low thickness. The most likely explanation appears to be displacement decoherence.[8] (While specimen drift has been identified as one possible cause, especially for exposure times longer than around ¼ s,[4] it would not produce the thickness-dependent effect we observe.)

From the earliest days of electron microscopy on amorphous materials,[22] a 'twinkling' (i.e. time dependence) of speckle patterns in real or reciprocal space was observed. Figure 6 shows examples of this 'twinkling' in amorphous Si. Rezikyan et al. introduced the concept of 'displacement decoherence' to connect the 'twinkling' effect to the FEM discrepancy in absolute scattering.[8] They presented experimental data and simulations showing that atom position changes during exposure could mimic the effect of spatial incoherence and explain the intensity anomaly. They considered several possible origins for the atom displacements, including beam damage and large athermal displacements. Because of the observed thickness dependence, we suggest that the best fit could be obtained by collective time-varying displacements (small rotations) of the local film structure due to irradiation – which we will call 'fluttering'. A compelling reason to conclude this is that the stiffness of a thin plate increases as the third power of its thickness, which would favour a steep reduction in the local rotations (arising in the so-called 'tympanic modes') as thickness increases. With higher amplitude fluttering at the lowest thickness, the FEM signal would decay just as observed in Figure 5.

Experimentally, a decay in the FEM signal is observed as the exposure time increases with a rapid hybrid-pixel array camera,[11] and this is also evident with a CMOS camera for a thin sample of a-Si in Figure 7.

What could stimulate the fluttering of the thinnest areas? As the beam changes intensity or moves to a new position, it creates temperature changes, in addition to residual beam-induced positive charge at the previously probed locations. Estimates of the local temperature rise from a focused beam in a thin film have been made using the Bethe continuous slowing-down approximation.[23] Assuming a beam current of 1 nA, a probe size of 20 Å, and an a-Si sample of thickness 5 nm, this predicts a temperature rise of only 2°C or 3°C, depending on the physical extent of the thin area. While these temperatures may seem small, the thermal stress during the transient rise is estimated to be ~0.5 MPa, which could easily buckle a thin foil. Fluttering would be associated with time-varying changes – sources could include beam motion due to stray fields or charging, or fluctuations due to thermal flicker noise ($1/f$ noise),[24] or beam position instabilities. Other possibilities to consider include Coulomb explosions from relatively rare Auger events, which can deposit huge energies in the neighbourhood of

the relaxing atom. The issue is worthy of more detailed study, especially with a fast and efficient pulse-counting, hybrid-pixel array detector.

7 | CONCLUSIONS

There are two significant conclusions. The first concerns the effect of the pixelation and point spread function of a detector used for fluctuation electron microscopy. It has perhaps gone unnoticed before that even for a perfectly efficient pixelated detector, there is an intrinsic cutoff spatial frequency in nanodiffraction patterns because frequencies higher than $1/x_p$ (where the pixel size is x_p) are excluded from the data. This violates our assumption that for a random object, the mean value of variance is unity, and must account for some of the attenuation of the background level arising from random alignments. The effect is magnified if the camera point-spread function causes leakage into adjacent pixels, increasing the effective pixel size. For typical optically coupled CCD or CMOS cameras, the point-spread function is often about ten or more pixels FWHM. Provided the signal from any medium-range order in FEM is contained well within the band-pass of the detector (in other words larger in q-space than the point spread function), the peak heights over the background are not significantly affected, but they should be reported relative to the background and not relative to the $V = 0$ axis,[16] as has commonly been done. By choosing the optimal-sampling camera length and reporting only the background-subtracted peak-height, this effect of pixel leakage on the statistics used in FEM can be made small and more reproducible. The introduction of higher-performance direct electron detectors with narrow point-spread functions will undoubtedly improve the experimental situation, although inevitable pixelation must still be considered in the statistics.

Adding shot noise to the consideration, pixelation and the point-spread function can account for the need to reduce the magnitude of the term used to subtract noise that depends on the average scattered intensity. We show how this can be done quite reliably, ensuring that shot noise does not negatively impact the interpretation of background-subtracted peak heights.

Our second conclusion relates to the thickness dependence of the FEM normalised variance as a function of specimen thickness, using data from eleven different samples of a-Si, each prepared from different starting materials. We saw that for a-Si in the 80 keV electron studies, above a thickness of ~200 Å, the background-subtracted normalised variance follows the expected $1/t$ trend seen in simulations.[16] However, for thinner samples, thicknesses $\lesssim$ 200 Å, the normalised variance *decreases* with thickness, contrary to expectations. This anomalous behaviour must be considered when comparing samples, either to simulations or to each other, at least by fixing the thickness at a single value for comparisons. We speculate that the origin of this phenomenon is displacement decoherence arising from 'fluttering' of the thinnest areas of the sample. This issue warrants further detailed investigation as it may affect quantitative microscopy studies, other than FEM, of intensities in thin areas of samples. This will be the subject of future research.

ACKNOWLEDGEMENTS

The authors gratefully acknowledge support from the FAMU-FSU College of Engineering and the Department of Physics at the University of Vienna. This work was supported in part by funds from the National Science Foundation (NSF Award Number 1906367). Electron microscopy was performed at the National High Magnetic Field Laboratory, which is supported by National Science Foundation Cooperative Agreement No. DMR-2128556 and the State of Florida. Assistance from Yan Xin (MagLab), and Kevin McIlwarth & Nathaniel Didier (JEOL Inc) in configuring the JEOL ARM200F was invaluable. JMG is particularly grateful to Zhiyong 'Richard' Liang, Director of the High-Performance Materials Institute at Florida State University, for his advice and support. Early work was carried out with the Nion UltraSTEM at the University of Vienna, Faculty of Physics and the authors thank Andreas Berger, Alissa Freilinger, Jani Kotakoski, Clemens Mangler and Toma Susi for their advice and assistance.

ORCID

J. M. Gibson https://orcid.org/0000-0003-2519-0528
M. M. J. Treacy https://orcid.org/0000-0002-6552-1363

REFERENCES

1. Cheng, J. Y., Gibson, J. M., & Jacobson, D. C. (2001). Observations of structural order in ion-implanted amorphous silicon. *Journal of Materials Research*, *16*(11), 3030–3033.
2. Treacy, M. M. J., Kumar, D., Rougee, A., Zhao, G., Buseck, P. R., McNulty, I., Fan, L., Rau, C., & Gibson, J. M. (2007). Probing medium-range structural correlations by fluctuation microscopy. *Journal of Physics-Condensed Matter*, *19*(45), 455201.
3. Daulton, T. L., Bondi, K. S., & Kelton, K. F. (2010). Nanobeam diffraction fluctuation electron microscopy technique for structural characterization of disordered materials-Application to Al88-xY7Fe5Tix metallic glasses. *Ultramicroscopy*, *110*(10), 1279–1289.
4. Bogle, S. N., Nittala, L. N., Twesten, R. D., Voyles, P. M., & Abelson, J. R. (2010). Size analysis of nanoscale order in amorphous materials by variable-resolution fluctuation electron microscopy. *Ultramicroscopy*, *110*(10), 1273–1278.
5. Yi, F., & Voyles, P. M. (2011). Effect of sample thickness, energy filtering, and probe coherence on fluctuation electron microscopy experiments. *Ultramicroscopy*, *111*(8), 1375–1380.

6. Lee, B.-S., Darmawikarta, K., Raoux, S., Shih, Y.-H., Zhu, Y., Bishop, S. G., & Abelson, J. R. (2014). Distribution of nanoscale nuclei in the amorphous dome of a phase change random access memory. *Applied Physics Letters*, *104*(7), 071907.
7. Radić, D., Hilke, S., Peterlechner, M., Posselt, M., & Bracht, H. (2019). Fluctuation electron microscopy on silicon amorphized at varying self ion-implantation conditions. *Journal of Applied Physics*, *126*(9), https://doi.org/10.1063/1.5107494
8. Rezikyan, A., Jibben, Z. J., Rock, B. A., Zhao, G., Koeck, F. A. M., Nemanich, R. F., & Treacy, M. M. J. (2015). Speckle suppression by decoherence in fluctuation electron microscopy. *Microscopy and Microanalysis*, *21*(6), 1455–1474.
9. Li, T. T., Bogle, S. N., & Abelson, J. R. (2014). Quantitative fluctuation electron microscopy in the STEM: Methods to identify, avoid, and correct for artifacts. *Microscopy and Microanalysis*, *20*(5), 1605–1618.
10. Radic, D., Hilke, S., Peterlechner, M., Posselt, M., Wilde, G., & Bracht, H. (2020). Comparison of experimental STEM conditions for fluctuation electron microscopy. *Microscopy and Microanalysis*, *26*(6), 1100–1109.
11. Zjajo, A., Du, H., Dunin-Borkowski, R. E., Gibson, J. M., Rezikyan, A., & Treacy, M. M. J. (2025). Rapid-acquisition fluctuation electron microscopy: Decoherence and the dominant role of noise. *Microscopy and Microanalysis*, *31*(3), ozaf049.
12. Vulovic, M., Rieger, B., van Vliet, L. J., Koster, A. J., & Ravelli, R. B. G. (2010). A toolkit for the characterization of CCD cameras for transmission electron microscopy. *Acta Crystallographica Section D-Structural Biology*, *66*(1), 97–109.
13. Battaglia, M., Contarato, D., Denes, P., Doering, D., Duden, T., Krieger, B., Giubilato, P., Gnani, D., & Radmilovic, V. (2010). Characterisation of a CMOS active pixel sensor for use in the TEAM microscope. *Nuclear Instruments and Methods in Physics Research Section A: Accelerators, Spectrometers, Detectors and Associated Equipment*, *622*(3), 669–677.
14. Tate, M. W., Purohit, P., Chamberlain, D., Nguyen, K. X., Hovden, R., Chang, C. S., Deb, P., Turgut, E., Heron, J. T., Schlom, D. G., Ralph, D. C., Fuchs, G. D., Shanks, K. S., Philipp, H. T., Muller, D. A., & Gruner, S. M. (2016). High dynamic range pixel array detector for scanning transmission electron microscopy. *Microscopy And Microanalysis*, *22*(1), 237–249.
15. Treacy, M. M. J., & Gibson, J. M. (1996). Variable coherence microscopy: A rich source of structural information from disordered materials. *Acta Crystallographica Section A*, *52*, 212–220.
16. Treacy, M. M. J., & Gibson, J. M. (2012). Examination of a polycrystalline thin-film model to explore the relation between probe size and structural correlation length in fluctuation electron microscopy. *Microscopy and Microanalysis*, *18*(1), 241–253.
17. Gibson, J. M., & Treacy, M. M. J. (2017). Fluctuation microscopy analysis of amorphous silicon models. *Ultramicroscopy*, *176*(SI), 74–79.
18. Gibson, J. M., Elliman, R., Susi, T., & Mangler, C. (2025). Self-ion implantation and structural relaxation in amorphous silicon. arXiv:2506.00176.
19. Fan, L., Paterson, D., McNulty, I., Treacy, M. M. J., & Gibson, J. M. (2007). Fluctuation X-ray microscopy: A novel approach for the structural study of disordered materials. *Journal of Microscopy-Oxford*, *225*(1), 41–48.
20. Levin, B. D. A. (2021). Direct detectors and their applications in electron microscopy for materials science. *Journal of Physics: Materials*, *4*(4), 042005.
21. Takeuchi, Y., & Inaba, M. (1991). Measurement of silicon native oxide thickness by XPS. *Analytical Sciences*, *7*(S), 333–334.
22. Howie, A., Krivanek, O., & Rudee, M. (1973). Interpretation of electron micrographs and diffraction patterns of amorphous materials. *Philosophical Magazine*, *27*(1), 235–255.
23. Reimer, L. (1984). *Transmission electron microscopy: Physics of image formation and microanalysis*. Springer-Verlag.
24. Knapek, A., Grmela, L., Sikula, J., & Sik, O. (2012). Cold field-emission cathode noise analysis. *Metrology and Measurement Systems*, *19*(2), 417–422.

How to cite this article: Gibson, J. M., & Treacy, M. M. J. (2025). Quantitative corrections for fluctuation electron microscopy. *Journal of Microscopy*, *300*, 356–365. https://doi.org/10.1111/jmi.70027